

All-Atom Stability and Oligomerization Simulations of Polyglutamine Nanotubes with and without the 17-Amino-Acid N-Terminal Fragment of the Huntingtin Protein

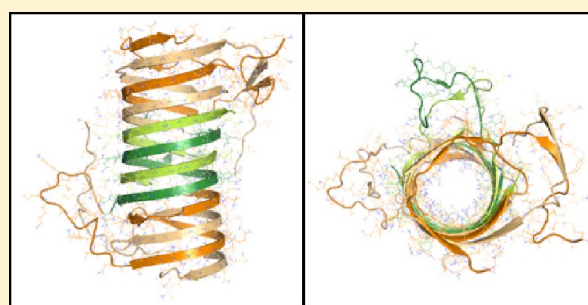
Sébastien Côté,[†] Guanghong Wei,[‡] and Normand Mousseau^{*,†}

[†]Département de Physique and Groupe de recherche sur les protéines membranaires (GEPROM), Université de Montréal, C.P. 6128, succursale Centre-ville, Montréal (Québec), Canada

[‡]State Key Laboratory of Surface Physics and Department of Physics, Fudan University, 220 Handan Road, Shanghai, 200433, China

S Supporting Information

ABSTRACT: Several neurodegenerative diseases are associated with the polyglutamine (polyQ) repeat disorder in which a segment of consecutive glutamines in the native protein is produced with too many glutamines. Huntington's disease, for example, is related to the misfolding of the Huntingtin protein which occurs when the polyQ segment has more than approximately 36 glutamines. Experimentally, it is known that the polyQ segment alone aggregates into β -rich conformations such as amyloid fibrils. Its aggregation is modulated by the number of glutamine residues as well as by the surrounding amino acid sequences such as the 17-amino-acid N-terminal fragment of Huntingtin which increases the aggregation rate. Little structural information is available, however, regarding the first steps of aggregation and the atomistic mechanisms of oligomerization are yet to be described. Following previous coarse-grained replica-exchange molecular dynamics simulations that show the spontaneous formation of a nanotube consisting of two intertwined antiparallel strands (Laghaei, R.; Mousseau, N. *J. Chem. Phys.* **2010**, *132*, 165102), we study this configuration and some extensions of it using all-atom explicit solvent MD simulations. We compare two different lengths for the polyQ segment, 40 and 30 glutamines, and we investigate the impact of the Huntingtin N-terminal residues (htt^{NT}). Our results show that the dimeric nanotubes can provide a building block for the formation of longer nanotubes (hexamers and octamers). These longer nanotubes are characterized by large β -sheet propensities and a small solvent exposure of the main-chain atoms. Moreover, the oligomerization between two nanotubes occurs through the formation of protein/protein H-bonds and can result in an elongation of the water-filled core. Our results also show that the htt^{NT} enhances the structural stability of the β -rich seeds, suggesting a new mechanism by which it can increase the aggregation rate of the amyloidogenic polyQ sequence.



INTRODUCTION

Several neurodegenerative diseases are characterized by protein misfolding leading to β -sheet-rich insoluble amyloid deposits in brain tissues.^{1–3} For instance, trinucleotide CAG/polyQ repeat disorders are at the origin of such misfolding for at least nine proteins when the repeat length exceeds a sequence-dependent threshold.^{4–6} Of those nine, the Huntingtin protein misfolds when the native segment of consecutive glutamines at its N-terminal has at least 36 glutamines, forming structures associated with the pathology of the Huntington disease.⁷ To unveil the molecular mechanisms behind Huntingtin aggregation, most studies have focused on the Huntingtin exon 1, which can cause neurological phenotype *in vivo* by itself,⁸ or on fragments of this exon. The Huntingtin exon 1 has an amphipathic N-terminal of 17 residues (htt^{NT}), followed by a segment of consecutive glutamines (polyQ), a segment of consecutive prolines (polyP), and a proline-rich segment.

The aggregation of polyQ alone has been intensively studied,⁹ as it is the only segment sharing high sequence

homology through the nine proteins affected by the polyQ repeat disorder. Early studies postulated different and sometimes conflicting structural models for the fibrils.¹⁰ For instance, X-ray scattering results were interpreted as polyQ aggregating into either β -rich amyloid fibrils characterized by polar zippers¹¹ or water-filled nanotubes.¹² This latter model was later reinterpreted as stacked β -sheets composed of β -hairpin motifs.¹³ Compact β -sheet models characterized by antiparallel strand-turn-strand motifs with each strand being composed of 7–9 glutamines were also suggested from mutagenesis studies.¹⁴ Interestingly, this model induces cell toxicity when enforced in the polyQ sequence of the Huntingtin exon 1 N-terminal.¹⁵ Compatible with the compact β -sheet models, slab-like β -sheet structures were proposed from X-ray scattering experiments.¹⁶ More recently, solid-state NMR spectroscopy

Received: July 5, 2012

Revised: September 14, 2012

Published: September 15, 2012

Table 1. Summary of All MD Simulations^a

simulation name	temp (K)	time (ns)	box type	box vector lengths (nm)	no. of water molecules
Q ₄₀ X2	300	250	octahedron	$a = b = c = 8$	11 566
htt ^{NT} Q ₄₀ X2	300	250	cubic	$a = b = c = 12$	56 381
Q ₄₀ X6	300	250	rectangular	$a = b = 7, c = 9$	13 278
htt ^{NT} Q ₄₀ X6	300	250	cubic	$a = b = c = 14$	88 662
Q ₄₀ X6_330K	330	250 × 2	rectangular	$a = b = 7, c = 9$	13 278/13 286
Q ₃₀ X2	300	250	octahedron	$a = b = c = 7.8$	10 762
htt ^{NT} Q ₃₀ X2	300	250	cubic	$a = b = c = 12$	56 504
Q ₃₀ X8	300	250	rectangular	$a = b = 9, c = 11$	28 149
htt ^{NT} Q ₃₀ X8	300	250	cubic	$a = b = c = 14$	88 409
Q ₃₀ X8_330K	330	250 × 2	rectangular	$a = b = 9, c = 11$	28 149/28 131
Q ₄₀ X6_Oligo1	300	200	cubic	$a = b = c = 11$	42 596
Q ₄₀ X6_Oligo2	300	200	cubic	$a = b = c = 11$	42 609
Q ₄₀ X6_Gromos	330	100	rectangular	$a = b = 7, c = 9$	13 329
Q ₄₀ X6_Amber	330	100	rectangular	$a = b = 7, c = 9$	13 312
Q ₄₀ X6_Charmm	330	100	rectangular	$a = b = 7, c = 9$	13 283

^aWe compare two lengths for the polyQ segment: 40 vs 30 glutamines per polypeptide chain, respectively designated as Q₄₀ and Q₃₀. We simulate dimeric nanotubes Q₄₀X2 and Q₃₀X2, and longer nanotubes—the hexamer Q₄₀X6 and the octamer Q₃₀X8, both counting 240 glutamines. The impact of the Huntingtin protein N-terminal is studied for every configurations (htt^{NT} Q_N). The growth of longer nanotubes is investigated twice in Q₄₀X6_Oligo. Finally, the stability of Q₄₀X6 is studied using Gromos53a6, Amber99sb-ILDN, or Charmm27 (Q₄₀X6_Gromos, Q₄₀X6_Amber, or Q₄₀X6_Charmm, respectively).

suggested that the fibrils of D₂Q₁₅K₂ fragments are composed of straight antiparallel β -sheets, while those of GK₂Q₃₈K₂ and GK₂Q₅₄K₂ peptides are respectively composed of sheet-bend-sheet and sheet-bend-sheet-bend-sheet motifs arranged in superpleated antiparallel cross- β .¹⁷

PolyQ segments as short as eight glutamines form mature fibrils *in vitro*¹⁸ through a nucleation-elongation process,¹⁹ even though the kinetics of fibril formation is repeat-length-dependent with longer polyQ segments being more prone to aggregate.²⁰ The nucleus size is also repeat-length-dependent, as it is characterized by a sharp transition from nucleus sizes of 4 for Q₂₃ to 1 for Q₂₆ and longer repeat lengths.²¹ It is, however, very challenging to experimentally characterize the structural features of the nucleus and the early on- and off-pathway aggregates to fibrillation. The difficulty resides mainly in the highly dynamical nature of these processes as the oligomeric species exist only in a complex dynamical equilibrium.

To complement experimental observations, these aspects have been investigated by computational studies. For instance, simulations showed that a parallel three-coiled circular water-filled β -helix with 18 or 20 residues per coil is unstable, while a parallel triangular β -helix with a dry core is stable.²² Other groups observed the formation and stability of parallel β -helices²³ and β -helical-like monomers.^{24,25} Other simulations showed that water-filled nanotubes made with parallel β -sheets decay into β -helical-like structures characterized by sheet-bend-sheet motifs.²⁶ Diverse slab-like aggregates of Q₁₅ and Q₆ with the polar zipper motif were very stable in all-atom simulations with explicit solvent representation.²⁷ Nucleation and length-dependent features of polyQ monomers,²⁸ as well as dimerization,²⁹ were also investigated.

The toxicity does not only solely depend on length-dependent structural features of polyQ;³⁰ the neighboring residues to the polyQ repeat strongly modulate its kinetics of aggregation,^{31,32} toxicity,³³ and subcellular localization.³⁴ For instance, expressing the polyP sequence of Huntingtin at the C-terminal of polyQ reduces the aggregation propensity,³⁵ while the presence of the first 17 amino acids (htt^{NT}) of Huntingtin

at the N-terminal of polyQ enhances the aggregation,³⁶ even in the presence of the C-terminal polyP sequence.³⁷ It has been postulated that the amphipathic character of the htt^{NT} would favor intermolecular interactions between the htt^{NT} bringing the polyQ segments in close contact.^{37,38} Such multidomain misfolding³⁹ would enhance the formation of aggregation-prone structural motifs in polyQ. Circular dichroism (CD) spectroscopy studies showed that the htt^{NT} populates α -helical structures.^{18,33,40} Computational studies on the monomer of htt^{NT} either show very high⁴¹ or moderate⁴² α -helical content. When linked to the polyQ segment, the htt^{NT} also populates α -helical structures, as shown by X-ray crystallography on exon 1 of Huntingtin⁴³ and CD experiments on htt^{NT} Q_N aggregates.¹⁸ Computational studies obtained more diverse results: it was shown that the htt^{NT} mostly populates a helix-kink-helix motif in the exon 1,⁴⁴ while the htt^{NT} Q_N monomer and dimer adopt rather amorphous configurations when the polyQ fragment consists of more than 20 glutamines.⁴⁵

In spite of these efforts, there has been few experimental or computational observations on the structural features of small oligomers of htt^{NT} Q_N. In the present study, we investigate such systems—dimers, hexamers, and octamers of Q_N and htt^{NT} Q_N for sequences containing 40 and 30 glutamines—using all-atom explicit solvent molecular dynamics (MD) simulations. Starting from the double-stranded antiparallel β -sheet nanotubes obtained previously in unbiased replica exchange molecular dynamics (REMD) simulations,⁴⁶ we confirm the stability of this fold, and study higher order aggregates composed of the same motif.

This article is constructed as follows. In the next section, we describe our methodology for the various simulations done. We then present our results by discussing the stability of the dimeric nanotube and the impact of the htt^{NT}. Further, we show that longer nanotubes with and without the htt^{NT} are significantly more stable than their dimeric counterpart, and we describe their growth mechanism. In the last section, we discuss our results in light of previous experimental and computational studies on the polyQ sequence and on the influence of the first 17 residues of the Huntingtin protein.

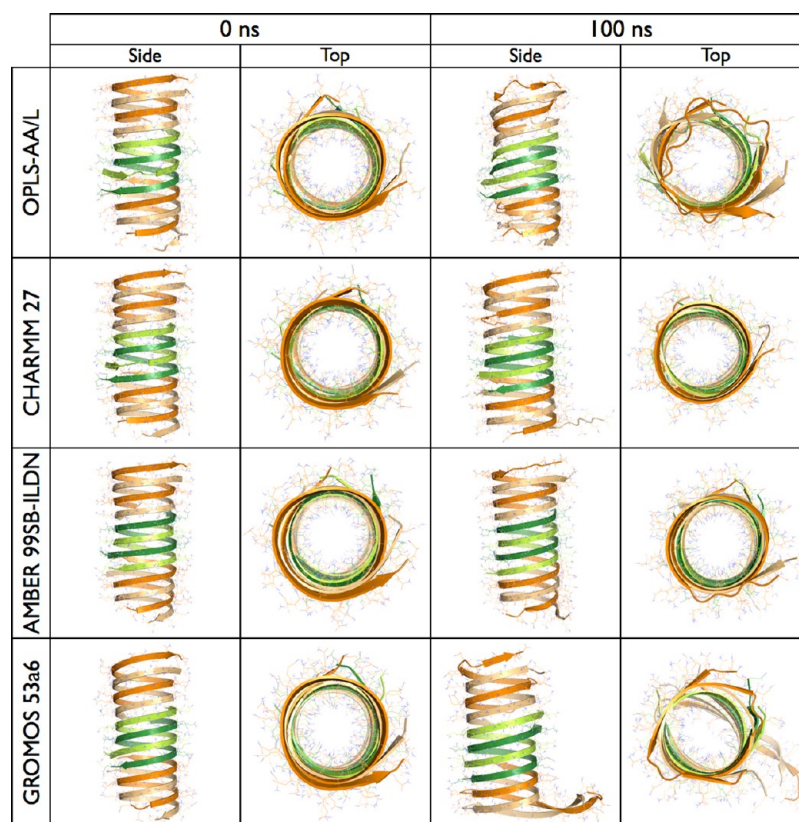


Figure 1. Snapshots of the $Q_{40}X_6$ nanotube. The side and top views at 0 and 100 ns using four different force fields at 330 K. From top to bottom, OPLS-AA/L, CHARMM27, AMBER99sb-ILDN, and GROMOS53a6. The side and top views are respectively displayed on the left and right columns for each time.

METHODOLOGY

In this study, we use an all-atom force field with an explicit solvent representation to test the stability of dimeric, hexameric, and octameric polyQ nanotubes, and to probe the growth of the hexameric polyQ nanotube. The building block for these folds is taken from unbiased coarse-grained replica exchange molecular dynamics (REMD) simulations performed by our group.⁴⁶ These simulations lead to the spontaneous formation of a dimeric antiparallel polyQ nanotube, which was found to be stable only for chains of more than 35 glutamines. Here, starting from the nanotube obtained for Q_{40} , we investigate its stability at an all-atom level, and compare against similar structures built with Q_{30} . For both chain lengths, we also examine the effect of the Huntingtin protein N-terminal, MATLEKLMKAFESLKSF (residues 1–17, htt^{NT}) on the stability of the nanotube assemblies. These extensive molecular dynamics simulations totalizing 3.7 μ s are summarized in Table 1.

Structures of Assemblies. All polyQ folds presented in this study are based upon the results of previous REMD simulations performed with a coarse-grained protein force field.⁴⁶ From a completely random initial structure, we observed the spontaneous formation of a nanotube composed of two intertwined Q_{40} polypeptide chains, and characterized by an antiparallel β -sheet with 0.68 H-bonds per residue. Reconstruction to all-atom of the coarse-grained side-chains was performed with SCRWL4,⁴⁷ which determines the best side-chain arrangement from the backbone configurations. In the rest of this paper, the reconstructed original nanotube is designated by $Q_{40}X_2$. The structure of $Q_{30}X_2$ was then

obtained from $Q_{40}X_2$ by removing 10 glutamine residues at the C-terminal of each chain. Both Q_{40} and Q_{30} dimers were used as building blocks to assemble longer nanotubes: hexamers for Q_{40} and octamers for Q_{30} , both structures consisting of the same number of glutamine residues and winding turns. To assemble these longer nanotubes, the dimers were positioned by hand in such a way as to maximize main-chain/main-chain hydrogen bonding. For the simulations on the impact of the htt^{NT}, we added this 17-residue sequence to the N-terminal of each polypeptide chain in all of these structures. The htt^{NT} fragment is initially completely extended without any secondary structure element, and it is positioned orthogonally to the nanotube axis.

MD Simulations. All simulations are performed in the NPT ensemble using Gromacs version 4.5.4^{48–51} with the OPLS-AA/L force field^{52,53} and the TIP4P⁵⁴ explicit solvent representation. Prior to launching the MD simulations, bad contacts in the reconstructed structures are first removed by energy minimization using the conjugate gradient method with a steepest descent method applied at every 100 steps. Second, structures are solvated and, for the models with the htt^{NT}, two chloride ions per polypeptide chain are added to neutralize the system. Third, the solvated structures are again energy-minimized using the same protocol as described above for the solvent-free case. Fourth, the systems are thermalized at 300 or 330 K for 1 ns using an integration step of 1 fs with position restraints on the protein heavy atoms. Finally, the system is equilibrated at a pressure of 1 atm for 1 ns using an integration time step of 1 fs with position restraints on the heavy atoms of

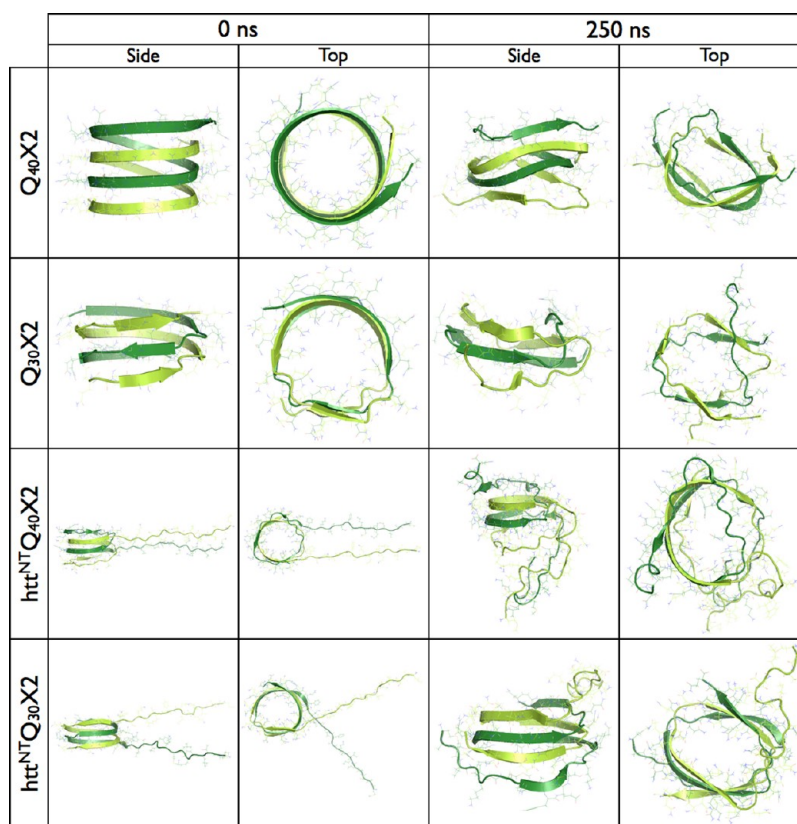


Figure 2. Snapshots of the dimeric nanotubes. The side and top views at 0 and 250 ns of Q₄₀X2 and Q₃₀X2 are respectively shown on the first and second rows. Structures with the htt^{NT} are shown on the third and fourth rows for htt^{NT}Q₄₀X2 and htt^{NT}Q₃₀X2, respectively. The side and top views are respectively displayed on the left and right columns for the initial and final states.

the protein. The conformations at 0 ns in all figures refer to the structures obtained after these pre-MD steps.

Bond lengths of the peptides are constrained with LINCS,⁵⁵ and water geometries with SETTLE,⁵⁶ allowing an integration time step of 2 fs. The solute and solvent are separately coupled to external temperature and pressure baths. The temperature of the systems is maintained at 300 or 330 K using the velocity rescaling thermostat⁵⁷ with a coupling constant of 0.1 ps. The pressure is isotropically coupled to 1 atm using the Parrinello–Rahman barostat^{58,59} with a coupling constant of 2 ps. The particle-mesh Ewald (PME) method^{60,61} is used to calculate the electrostatic interactions with a real space cutoff of 1.0 nm. The cutoff is 1.4 nm for the van der Waals interactions. The neighbor list is updated every 20 fs. The center-of-mass motion of the solute is removed every 10 ps. Conformations are saved every 10 ps. The other relevant parameters such as the temperature, the simulation time, the box type, the box vector lengths, and the number of water molecules for each simulation are shown in Table 1.

To ensure that the box size for each simulation is large enough to avoid any self-interaction through the periodic boundary conditions, the minimum distance between the peptide and its adjacent periodic images is always greater than 2 nm. By checking the structural stability of Q₄₀X6 using four different force fields—OPLS-AA/L,^{52,53} Gromos53a6,⁶² CHARMM27,^{63,64} and Amber99sb-ILDN⁶⁵—we found that our results are mostly force field independent. As shown in Figure 1, the nanotube is stable over 100 ns at the relatively high temperature of 330 K for all of these force fields. More precisely, the nanotube is most stable when parametrized with

the all-atom CHARMM27 force field than with OPLS-AA/L, which we use in the rest of this study, and AMBER99sb-ILDN. The edges of the nanotube are least stable with the united-atom GROMOS53a6 force field. Another simulation on the dimeric nanotube Q₄₀X2 using CHARMM27 also confirms its stability at 300 K for 250 ns during which the average β -sheet content is $83 \pm 3\%$ (vs $57 \pm 4\%$ when using OPLS-AA/L).

Analysis. Data analysis is performed with the Gromacs facilities and our in-house codes. To compare the results of Q₄₀ with Q₃₀, and to evaluate the impact of the htt^{NT}, we compute a number of quantities: the number of hydrogen bonds, the root-mean-square deviations (rmsd) with respect to the initial structure, the solvent accessible surface area (SASA),⁶⁶ the contact propensities, and the content of secondary structure (using STRIDE⁶⁷). A contact between two nonconsecutive residues is considered present when two aliphatic carbons are within 4.8 Å or when any two other atoms are within 5.4 Å of each other.⁶⁸ To remove the high frequency thermal fluctuations, all the data reported as a function of time are computed as a running-time average over 5 ns windows.

Convergence is assessed by tracking the backbone root-mean-square deviation (BB-rmsd) as well as by following other relevant parameters such as the number of hydrogen bonds, the SASA of the backbone atoms, and the secondary structures. We run each simulation long enough to ensure that the last 100 ns is converged as shown in Figure S1 (Supporting Information). Accordingly, averages and standard deviations on the BB-rmsd, the percentage of secondary structure, the number of hydrogen bonds, the number of contacts, and the SASA are computed, in all cases, over the interval 150–250 ns. Error bars are the

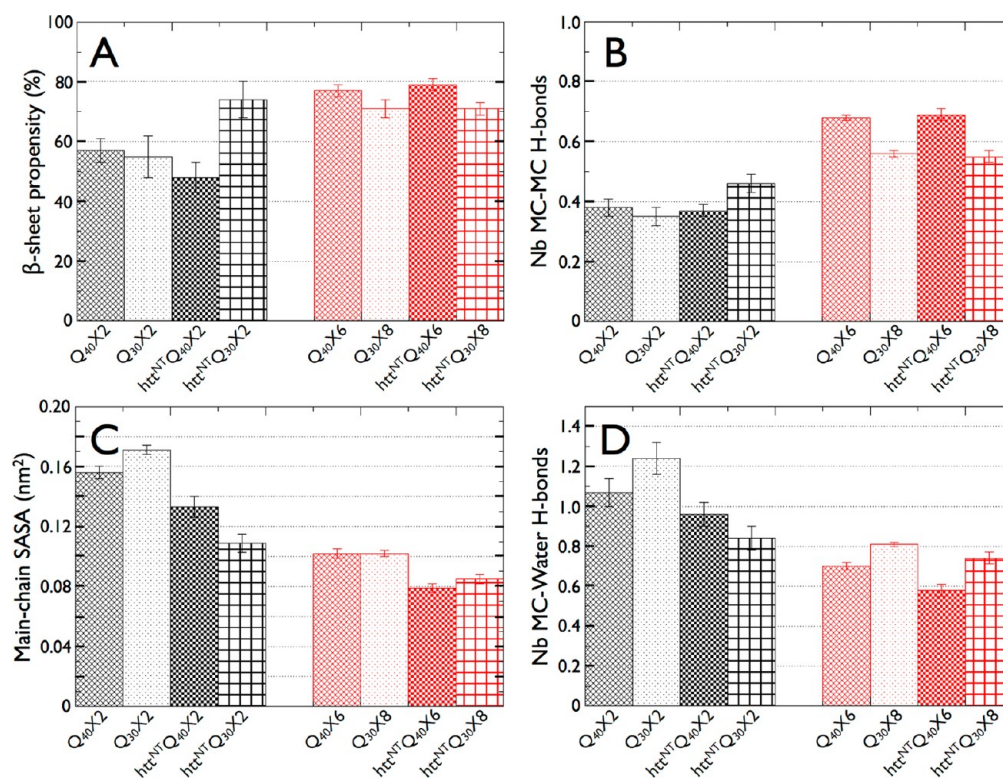


Figure 3. Mean values and standard deviations over the glutamine residues of various structural properties of the nanotubes in the converged time interval (150–250 ns). β -sheet propensity (panel A), number of main-chain/main-chain H-bonds per residue (panel B), SASA per residue of the main-chain atoms (panel C), and number of main-chain/water H-bonds per residue (panel D) for the various systems studied here. Higher stability of the nanotube core is correlated to a greater β -sheet content and a larger number of main-chain/main-chain H-bonds, as well as a smaller SASA of the main-chain atoms and a smaller number of main-chain/water H-bonds. The values for the dimers are shown to the left (black), and the values for the longer nanotubes are shown to the right (red). The standard deviations are displayed by error bars.

standard deviations of these quantities. Finally, molecular graphics images are generated using the PyMOL software (<http://www.pymol.org>).

RESULTS

Simulations on the Dimeric Nanotubes. *Q₄₀X₂* and *Q₃₀X₂*. The top and side views of the *Q₄₀X₂* and *Q₃₀X₂* nanotubes at 0 and 250 ns are shown in Figure 2. After 250 ns, they are still aggregated with no segment interacting preferentially with water molecules. They remain in their original antiparallel arrangement with a significant propensity for β -sheet: $57 \pm 4\%$ for *Q₄₀* and $55 \pm 7\%$ for *Q₃₀* (Figure 3, panel A). As a result, the backbone (BB-) rmsd, computed with respect to the initial structure, converges at 4.4 ± 0.2 Å for *Q₄₀X₂* and 4.0 ± 0.4 Å for *Q₃₀X₂* (Figure 4). The water-filled core of *Q₄₀X₂* collapses at 190 ns due to the formation of protein/protein H-bonds there, while it remains preserved in *Q₃₀X₂*. As discussed in the next section, the water-filled core stability increases significantly with the nanotube length.

To assess the impact of the chain length on the dimeric nanotubes, we computed quantities related to their stability such as the average β -sheet content, the number of main-chain/main-chain and main-chain/water H-bonds, and the SASA of the main-chain atoms (Figure 3). Analysis of these quantities shows only slight differences between *Q₄₀X₂* and *Q₃₀X₂*. In terms of the β -sheet content, for example, while the propensity is slightly larger for *Q₄₀X₂*, the difference is not significant ($57 \pm 4\%$ vs $55 \pm 7\%$, panel A). A similar observation is made on the average number of main-chain/main-chain H-bonds per

residue: it is 0.38 ± 0.03 for *Q₄₀* compared to 0.35 ± 0.03 for *Q₃₀* (panel B). In line with these results, the SASA of the main-chain atoms and the number of main-chain/water H-bonds is smaller for *Q₄₀* (0.156 ± 0.004 nm² vs 0.171 ± 0.003 nm² from panel C and 1.07 ± 0.07 vs 1.21 ± 0.08 from panel D, respectively). All of these data suggest that *Q₄₀* is slightly more stable than *Q₃₀*, although this difference is not really significant for the dimers.

htt^{NT}Q₄₀X₂ and *htt^{NT}Q₃₀X₂*. We now examine the effect of adding the Huntingtin N-terminal residues, htt^{NT}, to the polyQ chains in *Q₄₀X₂* and *Q₃₀X₂*. The 250 ns MD simulations show that the addition of the htt^{NT} has a positive impact on the stability of the nanotubes. As for the pure polyQ chains, no part of the polyQ sequence interacts preferentially with water molecules (Figure 2). Also, the nanotube core retains the antiparallel β -strand arrangement, with a significant β -sheet propensity of $48 \pm 5\%$ for *Q₄₀* and $74 \pm 6\%$ for *Q₃₀* (Figure 3, panel A). Both the water-filled cores of htt^{NT} *Q₄₀X₂* and of htt^{NT} *Q₃₀X₂* are preserved throughout the simulations, as opposed to *Q₄₀X₂* without the htt^{NT}. The BB-rmsd, calculated on the polyQ region only, is also reduced by 0.5 Å for *Q₄₀* and by 1.3 Å for *Q₃₀* (Figure 4).

The stabilizing effect of the htt^{NT} is also seen in other structural quantities. For instance, for the nanotube core, the SASA of the main-chain atoms and the number of main-chain/water H-bonds are both reduced when the htt^{NT} is present (panels C and D in Figure 3, respectively). In terms of β -sheet content and the number of main-chain/main-chain H-bonds, the *Q₄₀* nanotube shows little changes after the addition of the

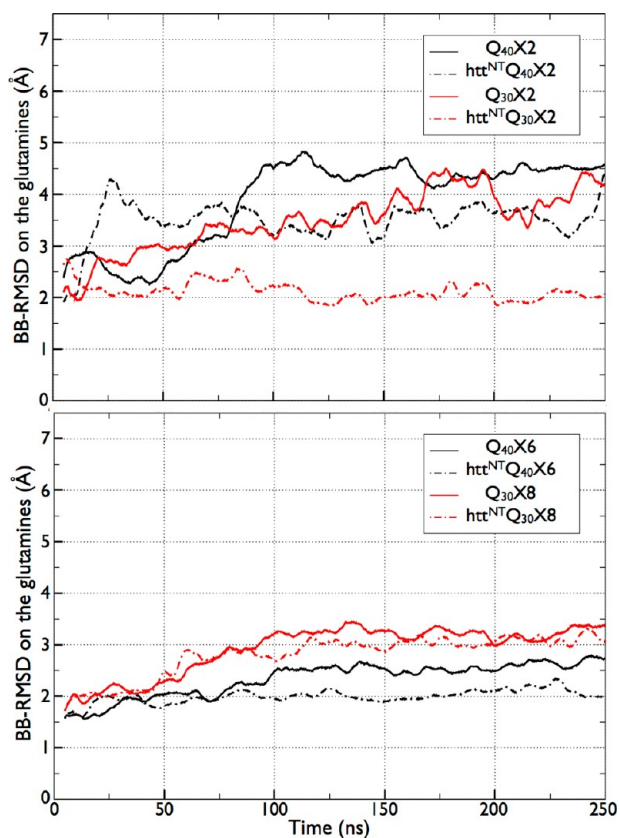


Figure 4. Time evolution of the backbone root-mean-square deviation (BB-rmsd) on the glutamine residues as measured with respect to the initial structure. The BB-rmsd is computed on the backbone atoms: O, N, C_{α} and C. The values for the dimers and the longer nanotubes are respectively shown on the top and bottom. The values for Q_{40} and Q_{30} are respectively displayed in black and red. The dotted lines represent the simulations with the htt^{NT} . Data are computed as a running-time average over 5 ns windows.

htt^{NT} , while these quantities show a significant increase for Q_{30} (panels A and B in Figure 3, respectively). This effect is directly associated with the refolding of the htt^{NT} at the end of the nanotube core, where it forms a β -sheet leading to an extension of the nanotube and fixing the polyQ chains into position. This motif appears very early in the simulation, at 14 ns, and it remains until the end of the run (Figure 2, dark green strand at the bottom of $htt^{NT} Q_{30}X2$'s side view at 250 ns).

The htt^{NT} segment itself does not display a well-defined structure. In our simulations, it populates isolated β -bridges, 3–10 helices, turns, and random coils but no α -helix for both Q_{40} and Q_{30} (Figure S2, Supporting Information). As discussed previously, the htt^{NT} in Q_{30} populates a β -sheet but not that in Q_{40} . In terms of contact propensity, the htt^{NT} of Q_{40} interacts mainly with itself and with the other htt^{NT} (77 ± 4), and less dominantly with the nanotube core (55 ± 4). For Q_{30} , the situation is reversed as one htt^{NT} participates in a β -sheet with the nanotube core: there are 44 ± 3 contacts between themselves and 92 ± 4 with the glutamine residues. The htt^{NT} also forms H-bonds with itself and the other htt^{NT} (14 ± 2 for Q_{40} and 6 ± 2 for Q_{30}), and with the glutamine residues (7 ± 2 for Q_{40} and 7 ± 1 for Q_{30}).

Simulations on the Longer Nanotubes. $Q_{40}X6$ and $Q_{30}X8$. We also simulated, at 300 and 330 K, longer nanotubes assembled from the dimers: hexamers for Q_{40} and octamers for

Q_{30} , both having 240 glutamines and the same number of winding turns. These structures are described in the Methodology section.

First, we present the simulations at 300 K and compare them to the dimers. After 250 ns, we clearly see that the longer nanotubes $Q_{40}X6$ and $Q_{30}X8$, with their water-filled core remaining intact throughout the simulations, are significantly more stable than their dimeric counterpart (Figure 5 vs Figure 2). Clearly, the BB-rmsd, computed with respect to the initial structure, supports this observation as it converges at 2.6 ± 0.1 Å for Q_{40} and 3.2 ± 0.2 Å for Q_{30} , which are smaller than the dimers' rmsd values by about 1–2 Å (Figure 4, bottom vs top panel). The propensity of β -sheet is also significantly larger for the longer nanotubes with $80 \pm 2\%$ for Q_{40} and $73 \pm 3\%$ for Q_{30} (Figure 3, panel A). Moreover, the main-chain/main-chain H-bond network, which is characteristic of the nanotube stability, is more protected from solvent when compared to the dimers. This is shown by a larger number of main-chain/main-chain H-bonds (panel B), a smaller SASA of the main-chain atoms (panel C), and a smaller number of main-chain/water H-bonds (panel D).

Comparing Q_{40} and Q_{30} more closely, we observe significant differences in terms of structural stability. As shown previously, the BB-rmsd is smaller for Q_{40} than Q_{30} (2.6 ± 0.1 Å vs 3.2 ± 0.2 Å, bottom panel in Figure 4), and Q_{40} has a larger β -sheet propensity than Q_{30} ($80 \pm 2\%$ vs $73 \pm 3\%$, Figure 3 on panel A). Also, the main-chain of Q_{40} forms more H-bonds with the other main-chains than Q_{30} (0.68 ± 0.01 vs 0.56 ± 0.01 from panel B) and less H-bonds with water molecules (0.70 ± 0.02 vs 0.81 ± 0.01 from panel D). As a result, the nanotube structure $Q_{40}X6$ is more ordered than that of $Q_{30}X8$ (Figure 5).

Further analysis at 330 K confirms the stability of the longer nanotubes. We did two independent simulations of 250 ns at 330 K for both $Q_{40}X6$ and $Q_{30}X8$. For each nanotube, two different initial structures were used: the same nanotubes as for the simulations at 300 K and a new nanotube for each chain length, assembled according to the prescription detailed in the Methodology section. The all-atom rmsd between the two initial structures is 3.8 Å for Q_{40} and 0.9 Å for Q_{30} , which is due to each dimer being rotated slightly differently with respect to each other along the nanotube central axis. These simulations confirm that, even at a relatively high temperature, the longer nanotubes are stable (Figure 6) as shown by the small BB-rmsd, which stays below 5 Å (Figure S3, Supporting Information). While the BB-rmsd are comparable for Q_{40} and Q_{30} , the latter structure is considerably more distorted and its water filled core is almost collapsed at 250 ns. For Q_{40} , some residues at one edge are detached from the nanotube after 200 ns due to the larger thermal fluctuations at the termini, while the middle subunit is very stable and undergoes small thermal fluctuations.

$htt^{NT} Q_{40}X6$ and $htt^{NT} Q_{30}X8$. After 250 ns, the longer nanotubes of Q_{40} and Q_{30} with the added htt^{NT} are still aggregated (Figure 5). Here again, the addition of the htt^{NT} plays a stabilizing role for the nanotube: the water-filled core remains intact, deformation over the simulation time-scale is minimal, and the BB-rmsd, computed from the initial structure on the glutamine residues, remains low (Figure 4, bottom panel). For Q_{40} , the BB-rmsd plateaus at 2.0 ± 0.1 Å, compared to 2.6 ± 0.1 Å for the pure polyQ sequence, while it remains mostly unchanged for Q_{30} (3.2 ± 0.2 Å compared to 3.1 ± 0.1 Å). The main-chain is also less accessible to the solvent (Figure 3, panel C), forming fewer hydrogen bonds with the water molecules (panel D). Internally, however, the structure is not

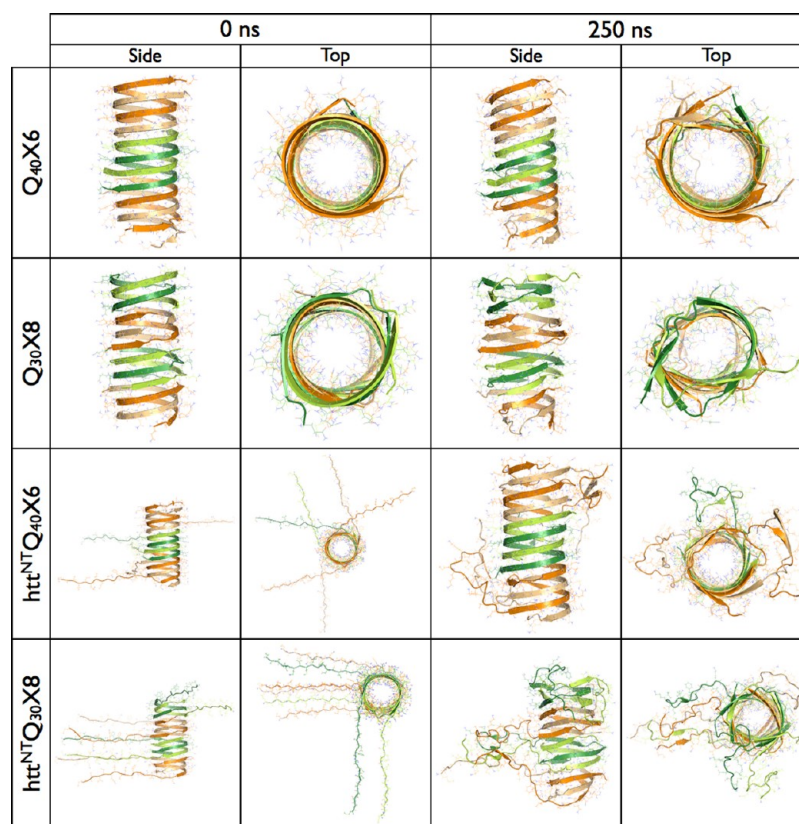


Figure 5. Snapshots of the longer nanotubes. The side and top views at 0 and 250 ns of Q₄₀X6 and Q₃₀X8 are respectively shown on the first and second rows. Structures with the htt^{NT} are shown on the third and fourth rows for htt^{NT} Q₄₀X6 and htt^{NT} Q₃₀X8, respectively. The side and top views are respectively displayed on the left and right columns for the initial and final states.

affected by the addition of the htt^{NT}: the β -sheet propensity (panel A) and the number of main-chain/main-chain H-bonds (panel B) are essentially identical with and without it. Overall, the htt^{NT} stabilizes the longer nanotube core by reducing the solvent exposure of the glutamines and the thermal fluctuations of the termini.

The structure of the htt^{NT} in the presence of the longer nanotubes is similar to that observed in the dimers. The segment populates the β -sheet, isolated β -bridge, turn, and random coil for both htt^{NT} Q₄₀X6 and htt^{NT} Q₃₀X8 (Figure S4, Supporting Information). A transient short 3–10 helix is also seen for Q₄₀, but no α -helix is observed over the time scale of our simulations. In terms of contact, the htt^{NT} interacts mostly intra- and intermolecularly with itself (202 ± 7 for Q₄₀ and 325 ± 10 for Q₃₀). Contacts are also observed, but to a lesser extent, between the htt^{NT} and the glutamine residues forming the nanotube core (200 ± 8 for Q₄₀ and 205 ± 9 for Q₃₀). On average, the htt^{NT} forms H-bonds in equal number with itself and with the others htt^{NT}, and with the glutamines for Q₄₀ (26 ± 4 and 26 ± 3 , respectively), while it much prefers self-contacts for the shorter polyQ sequence (40 ± 4 vs 25 ± 3), probably due to the higher ratio of htt^{NT} to the glutamines in the latter.

Formation of the Longer Nanotube. In the previous sections, we observed that the nanotube stability is significantly increased for longer nanotubes. We now investigate the process by which the nanotube Q₄₀X6 could be assembled from dimeric nanotubes in solution. We perform two independent simulations of 200 ns at 300 K on a system composed of a dimeric and a tetrameric nanotube, the latter providing a weakly

fluctuating seed to study oligomerization. These two simulations are launched from two different initial structures for which the position and the orientation of the dimer are varied with respect to the tetramer.

In the first system, the two nanotubes are positioned so as to avoid direct interactions between the dimer and the tetramer in the initial state, Q₄₀X6_Oligo1. The minimum distance between the two aggregates is 1.8 nm, and their respective nanotube axes are perpendicular to one another, as shown in Figure 7. In the same figure, we observe that at 63 ns the dimer binds to the tetramer through the formation of a single H-bond between the NH₂ group of a glutamine side-chain in the dimer and the C=O group of a glutamine main-chain in the tetramer. Once this H-bond forms, others are rapidly created between the dimer and the tetramer (Figure 8), aligning the axis of the dimeric nanotube toward that of the tetramer. The number of H-bonds between the two nanotubes increases to 7 at 100 ns. After 200 ns, the dimer and the tetramer share 18 H-bonds, the angle between their axis is $\sim 50^\circ$, and the total β -sheet propensity is 70%. We expect that longer simulations would allow further reorganizations to occur toward the nanotube Q₄₀X6, a very stable structure as discussed in the previous section (Figure 5) with a β -sheet propensity of $80 \pm 2\%$ (Figure 3, panel A).

For the second simulation, Q₄₀X6_Oligo2, we also ensure that there is no interaction between the dimeric and tetrameric nanotube initially, with a minimum distance of 1.8 nm between the two nanotubes. This time, however, they are positioned along the same axis and placed on top of each other (Figure S5, Supporting Information). At 40 ns, the dimer binds to the side

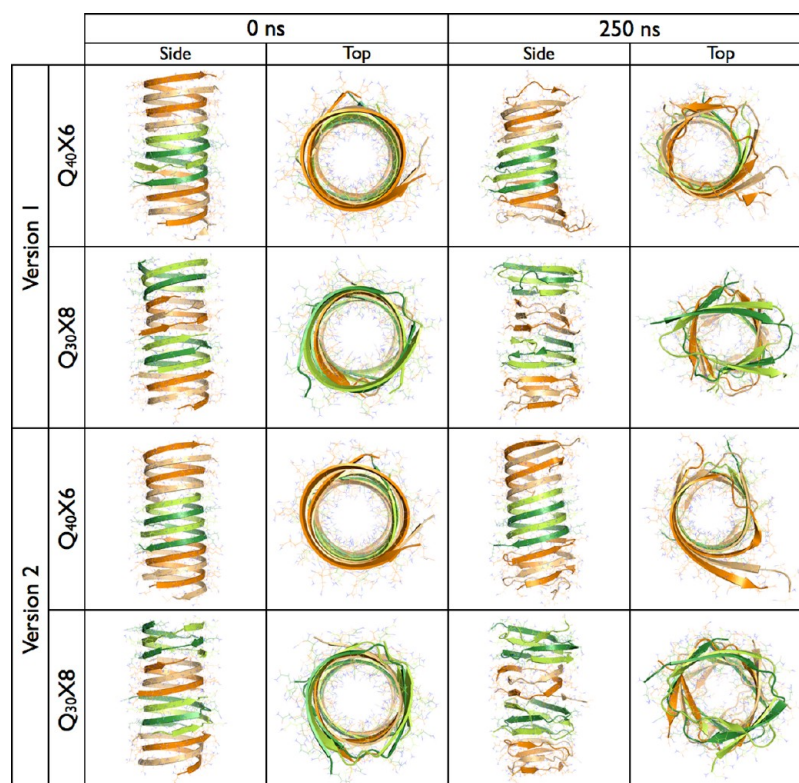


Figure 6. Snapshots of the longer nanotubes at 330 K. The side and top views at 0 and 250 ns of the simulations on Q₄₀X6 and Q₃₀X8 starting from two different initial structures, versions 1 and 2. The side and top views are respectively displayed on the left and right columns for the initial and final states.

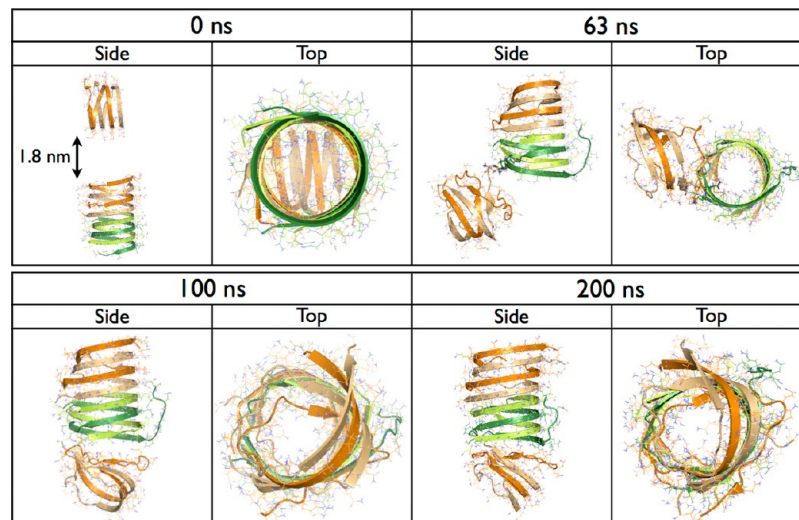


Figure 7. Snapshots during the Q₄₀X6_Oligo1 simulation. The side and top views at 0, 63, 100, and 200 ns during the oligomerization between a dimeric and a tetrameric nanotube. Initially, the two nanotubes are positioned at a minimum distance of 1.8 nm. At 63 ns, the dimer binds to the tetramer through the formation of a single H-bond, and further alignment of the dimeric nanotube axis to that of the tetramer follows.

of the tetramer nanotube through the formation of side-chain/side-chain H-bonds (Figure S6, Supporting Information). At 200 ns, the dimer is still attached on the side of the tetramer and both structures share 12 H-bonds, which is 6 H-bonds less than in Q₄₀X6_Oligo1. The total β -sheet propensity, however, is similar in both simulations (71% vs 70%). Unfortunately, it is not possible to quantitatively determine if one of the binding modes—on the top or on the side of the nanotube—is

energetically more favorable from our standard molecular dynamics simulations.

DISCUSSION

The Nanotube Configuration. In a previous study, we observed the spontaneous formation of a nanotube made of two antiparallel intertwined strands using replica exchange molecular dynamics (REMD) simulations coupled to a coarse-grained force field (Q₄₀ at 0 ns in Figure 2).⁴⁶ This structure is

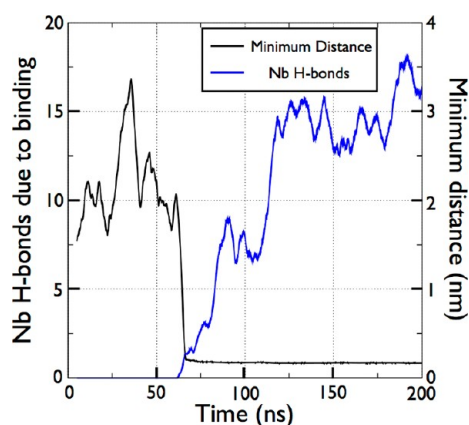


Figure 8. Time evolution of the number of hydrogen bonds between the dimeric and tetrameric nanotubes during the $Q_{40}X6_Oligo1$ simulation. The number of hydrogen bonds (left axis, blue) is correlated to the minimal distance between the dimer and the tetramer (right axis, black).

intrinsically different from the water-filled nanotube structure previously considered that is made of parallel nonintertwined strands.¹² Molecular dynamics simulations showed that the parallel nanotube model is unstable for the monomer,⁶⁹ and can decay toward β -helical-like structures with sheet-bend-sheet motifs.²⁶ Even if oligomeric parallel nanotubes are more stable, they still undergo large distortions within short time scale molecular dynamics (MD) simulations.^{70,71} Here, we show that the nanotubes made of antiparallel intertwined strands are stable over long time-scales using all-atom MD simulations with explicit solvent.

Indeed, the dimers remain folded for 250 ns (Figure 2), as shown by the small backbone root-mean-square deviation (BB-rmsd) with respect to the initial structure (Figure 4, top panel) and the large β -sheet propensity above 50% (Figure 3, panel A). While the dimers undergo some distortions, the longer nanotubes are significantly more stable (Figure 5), as shown by reduced BB-rmsd values (Figure 4, bottom panel), even at 330 K (Figure 6) and independently of the force field used (Figure 1). These longer nanotubes have also a larger β -sheet propensity ($80 \pm 2\%$ for $Q_{40}X6$ and $73 \pm 3\%$ for $Q_{30}X8$ from Figure 3 on panel A).

Recently, molecular structures of the $D_2Q_{15}K_2$, $GK_2Q_{38}K_2$, and $GK_2Q_{54}K_2$ fibrils have been proposed on the basis of solid-state NMR spectroscopy data.¹⁷ It was suggested that each strand is either extended ($D_2Q_{15}K_2$), extended-bend-extended ($GK_2Q_{38}K_2$), or extended-bend-extended-bend-extended ($GK_2Q_{54}K_2$). These motifs are arranged in antiparallel fashion along the fibril axis, an arrangement that shares structural features with our nanotube model. First, both structures are composed of antiparallel β -sheets. Second, our nanotube is made of sheet-bend-sheet motifs with each sheet consisting of ~ 17 residues (Figure S4, Supporting Information), which is similar to the ~ 15 residues observed by NMR and to the 7–9 residues hypothesized from mutagenesis results.¹⁴ Finally, the intertwined nanotube is similar to an out-of-registry fibril with a sheet-bend-sheet motif.

Whereas the fibril structures determined by solid-state NMR spectroscopy¹⁷ and X-ray scattering experiments^{11,16} are characterized by steric zipper structures with a dry core, the nanotubes studied here possess a water-filled core. In spite of these differences, these structures are stable at both 300 and

330 K for 250 ns (Figures 5 and 6, respectively). Moreover, the small variations shown by different structural properties of the nanotubes, particularly for the longer ones, over the last 100 ns confirm the convergence of our simulations (Figure S1, Supporting Information). Other all-atom MD simulations with explicit solvent show that the steric zipper structure with a dry core is also stable, at least over 50 ns.²⁷ Taken together, these results suggest that there exists a possible structural diversity for polyQ aggregates, at least for oligomers. Such structural diversity was previously confirmed for other amyloid sequences, which are expected to share high structural similarities despite their low sequence homology.¹ For instance, the amyloid-beta ($A\beta$) protein was shown to populate a wide range of fibrillar structures.^{72–74} Interestingly, a water-filled core structure was recently observed for $A\beta_{1-42}$ using cryo-electron microscopy (CryoEM)⁷⁵ and simulations.⁷⁶ As amyloid proteins are expected to share common structural features, water-filled structures cannot be ruled out for polyQ aggregates, and our results show that at least one nanotube structure—intertwined antiparallel strands—is stable. Of course, the polymorphism of $A\beta$ has been associated essentially with different quaternary arrangement of monomers with the same sheet-turn-sheet motif with a steric zipper.^{76,77} This motif appears driven by the many hydrophobic residues that need to be buried from the solvent. For polyQ, the polymorphism could be more diverse, as it is exclusively composed of hydrophilic glutamines which can form H-bonds either with other glutamines or with water molecules.

The growth of the longer nanotubes occurs via the formation of a single H-bond between two shorter nanotubes followed by the formation of other H-bonds favoring the alignment of the nanotubes along the tube axis (Figures 7 and 8). The shortest subunit of these longer assemblies is a dimeric nanotube whose formation was previously shown to occur in four main steps:⁴⁶ (1) apparition of extended regions in each monomer; (2) formation of antiparallel β -sheets; (3) structural reorganization occurring toward a water-filled triangular structure with sheet-bend-sheet motifs; (4) rearrangement into a nanotube as the triangular structure becomes cylindrical. Formation of extended regions in the monomers during the first step is critical to the formation of the nanotube. Interestingly, other simulations²⁸ also show that the formation of extended structures in the Q_{40} monomer is energetically unfavorable, agreeing with the monomeric nucleus size of 1 for Q_{40} observed experimentally.²¹ It is also compatible with a recent computational study showing that monomeric parallel nanotubes and steric zippers are not stable and that polyQ favors antiparallel conformations, such as β -sheet stacks.⁶⁵

It is also possible, on the other hand, that the nanotube structure is formed independently from the monomeric nucleus for two reasons. (1) It is not clear yet if the formation of polyQ oligomers can preclude nucleation or not,^{9,18,78} and (2) fibril-incompetent oligomers could also be populated during fibrillation, explaining the noninteger and negative nucleus sizes of Q_N and $htt^{NT}Q_N$ previously observed.⁷⁹

Effect of the Chain Length (Q_{40} vs Q_{30}). All polyQ repeat disorder diseases are characterized by a length-dependent pathological threshold on the polyQ segment.⁷ The disease occurs only for the protein containing a certain number of consecutive glutamines, and it occurs faster as the polyQ segment is longer. As the threshold depends on the native protein, being approximately 36 glutamines for Huntingtin, it cannot solely originate from the polyQ segment alone.³⁰ In fact,

β -sheet-rich fibrils are observed *in vitro* for polypeptide chains having as few as eight glutamines,¹⁸ with the aggregation being faster for longer polyQ segments.¹⁹

Previously, using a coarse-grained model, we showed that the nanotube composed of two intertwined antiparallel chains, which can spontaneously form for Q₄₀, is unstable when there is less than 35 glutamines.⁴⁶ Here, we reinvestigated the stability of the Q₃₀ dimeric nanotube using all-atom MD simulations with explicit solvent. In our simulations, Q₃₀X2 does not unfold after 250 ns and keeps its water-filled core (Figure 2), showing that water molecules and side-chain H-bonds are very important for stabilizing the nanotube structure of smaller chain lengths. The dimeric nanotube of Q₃₀ also keeps a large number of main-chain/main-chain H-bonds (Figure 3, panel B), and a high β -sheet propensity ($55 \pm 7\%$, from Figure 3 on panel A). For Q₄₀X2, these quantities are slightly larger, suggesting that the longer sequence forms a more stable nanotube. While this observation is not significant for the dimers, it is for the longer nanotubes Q₄₀X6 and Q₃₀X8 (Figure 3). Q₄₀X6 is also more ordered than the shorter sequence at both 300 K (Figure 5) and 330 K (Figure 6).

Our results are in agreement with other computational studies showing that longer polyQ segments are more ordered and favor dimerization. For instance, replica-exchange discrete molecular dynamics (RE-DMD) simulations coupled to a coarse-grained force field show that the formation of intermolecular H-bonds between polyQ segments is facilitated with longer repeat length in chymotrypsin inhibitor 2–polyQ chimeras.⁸⁰ Another DMD coarse-grained study on 24-mers of polyQ segment of diverse lengths showed that the β -sheet propensity and the aggregate stability increase for longer chain length.²⁵ These 24-mers formed annular, ring, and tube-like configurations.^{25,81} Finally, Monte Carlo simulations performed with an all-atom, implicit solvent force field showed that the probability of homodimerization of polyQ segments increases for longer chain length,²⁹ even though the sampled structures were mostly amorphous with very low secondary structure propensities.

Overall, simulations tend to show that both oligomerization and stability correlates with the number of glutamines in the polyQ segment in agreement with the increased rate of aggregation observed experimentally for the longer repeat length.¹⁹ These previous conclusions also apply to the intertwined antiparallel nanotube studied here.

Effect of the htt^{NT}. It is known that residues adjacent to the polyQ segment in the native protein strongly modulate the kinetics of aggregation.³¹ For instance, the presence of the first 17 amino acids of Huntingtin (htt^{NT}), an amphipathic segment, at the N-terminal of polyQ enhances oligomerization^{34,33} by favoring the appearance of intermolecular contacts between polyQ segments.^{18,36}

Here, we investigated the effect of the htt^{NT} on the dimeric nanotubes Q₄₀X2 and Q₃₀X2, as well as on the longer nanotubes Q₄₀X6 and Q₃₀X8. The htt^{NT} increases the dimers' stability by reducing the solvent accessibility of the glutamine residues (Figure 3 on panels C and D) and the thermal fluctuations at the polyQ N-terminal, as shown by the smaller BB-rmsd (Figure 4). It also helps to preserve the water-filled core of both Q₄₀X2 and Q₃₀X2. Interestingly, for the 30-residue polyQ sequence, the htt^{NT} forms a β -sheet with the glutamine residues of the nanotube core at 14 ns that remains present at 250 ns (Figure 2, dark green strand at the bottom of htt^{NT} Q₃₀'s side view at 250 ns). This motif greatly stabilizes the nanotube

core, as shown by a significant increase of β -sheet propensity ($55 \pm 7\%$ to $74 \pm 6\%$). Even if a similar motif is not observed for our Q₄₀ simulations, nothing prevents it from forming and helping to stabilize the nanotube structure during assembly. Similarly to the dimers, the longer nanotubes are also stabilized by the htt^{NT} (Figures 4 and 5) through a reduction of the solvent accessibility of the glutamine residues (Figure 3 on panels C and D) and the thermal fluctuations at the polyQ N-terminal.

In terms of secondary structures, the htt^{NT} shows a strong structural diversity as it populates turn, β -sheet, isolated β -bridge, and random coil in all structures (Figures S2 and S4, Supporting Information). We do not observe any α -helix on the time scale of our simulations, while CD spectroscopy experiments, for example, show that the htt^{NT} populates about $\sim 45\%$ helical configurations.³³ Aggregates of htt^{NT} Q_N are also found to populate α -helices with htt^{NT} Q₃₅K₂ having a percentage of $\sim 50\%$.¹⁸ Computational results are less conclusive, however. Replica exchange molecular dynamics (REMD) simulations combined with the AMBER03 all-atom implicit solvent force field show that the htt^{NT} in htt^{NT} Q₁₇P₁₁ and htt^{NT} Q₅₅P₁₁ mostly populates α -helices (50–80%) at 301 K, as well as 3–10 helices and turns to a lesser extent.⁴⁴ Similar results were obtained using simulated tempering (ST) simulations coupled to the AMBER03 force field on the htt^{NT} headpiece alone.²⁸ These simulations showed that it populates α -helices (20–80%) at 300 K, as well as 3–10 helices and turns to a lesser extent. On the other hand, bias exchange metadynamics (BEM) simulations with the all-atom AMBER99 force field and explicit solvent show that the htt^{NT} is mostly random coil with about $\sim 29\%$ α -helices.⁴² A replica-exchange discrete molecular dynamics (RE-DMD) simulation coupled to a coarse-grained model even showed that the htt^{NT} populates more extended (20–30%) than α -helical (5–10%) configurations in the exon 1 of Huntingtin.⁸² Mostly disordered aggregates were also observed for htt^{NT} Q_N using Monte Carlo simulations coupled to an all-atom force field with implicit solvent.⁴⁵ Overall, most studies tend to show that the htt^{NT} is structurally diverse, and populates α -helices to an extent that varies from one study to the other.

In line with those results, the htt^{NT} in our simulations populates different configurations such as 3–10 helix, turn, and random coil. However, it does not populate any α -helical configurations. To assess whether this absence is due to the presence of the nanotubes or is due to the sequence itself, we run a MD simulation at 300 K on a htt^{NT} monomer starting from a single α -helix configuration (data not shown). A running-time average on the percentage of α -helical content shows that the probability drops rapidly and remains low ($<5\%$) until 60 ns at which point the helix is completely unfolded. The probability of α -helix remains at 0% to the end of the simulation at 150 ns. The β -sheet propensity is also at 0% throughout the simulation. On the contrary, the htt^{NT} remains as a single α -helix to the end of the simulation at 150 ns when using CHARMM27 (data not shown), a force field that is known to bias toward α -helical configurations.^{83,84} Some of the computational studies mentioned earlier^{28,44} were also done using a force field that is known to bias toward α -helical configurations, AMBER03.⁸⁵ The complete determination of the structure of the htt^{NT} fragment will require a thorough investigation using new force fields such as CHARMM22* and AMBER99sb*-ILDN that have a better secondary structure balance.^{86–88}

Whether or not our selected force field underestimates the presence of α -helical structures in the htt^{NT}, our results show that this segment stabilizes the dimeric nanotube model studied here, which is composed of two intertwined antiparallel strands, and the longer nanotubes composed of these. The htt^{NT} could therefore favor oligomerization not only by bringing the glutamine segments close together, as suggested from experiments, but also by enhancing the stability of the β -sheet-rich seed as oligomerization occurs. It would be interesting to verify if such assertion is also observed for the polar zipper structure having the sheet-bend-sheet motif as recently determined by solid-state NMR spectroscopy.¹⁷

CONCLUSION

Although the existence of water-filled polyQ nanotubes is certainly not fully accepted today, growing evidence of polymorphism for other amyloid proteins such as amyloid-beta however suggests that this structure cannot yet be ruled out.^{74–76} Unbiased simulations have shown the spontaneous formation of a double-stranded antiparallel β -sheet nanotube.⁴⁶ The all-atom MD simulations with explicit solvent presented here show that this structural model serves as a building block to form longer nanotubes with higher structural stability. Molecular dynamics simulations for stability check using various well-known force fields confirm that these results are not an artifact. Moreover, all assemblies are stabilized by the first 17 amino acids of the Huntingtin protein (htt^{NT}), enhancing the stability of the β -sheet-rich seeds as oligomerization occurs. This latter observation suggests that the role of the htt^{NT} segment in increasing the aggregation rate of polyQ may be more diverse than previously thought, and shows that more experimental and computational studies are needed to better characterize its role at the atomic level.

ASSOCIATED CONTENT

Supporting Information

Figures showing the time evolution of various structural properties of the nanotubes, per residue secondary structures of the dimeric nanotubes, time evolution of the BB-rmsd of the longer nanotubes at 330 K, per residue secondary structures of the longer nanotubes, snapshots during the Q₄₀X6_Oligo2 simulation, and time evolution of the number of H-bonds during the Q₄₀X6_Oligo2 simulation. This material is available free of charge via the Internet at <http://pubs.acs.org>.

AUTHOR INFORMATION

Corresponding Author

*E-mail: normand.mousseau@umontreal.ca.

Notes

The authors declare no competing financial interest.

ACKNOWLEDGMENTS

This work was funded in part by the Canada Research Chairs program, the Fonds québécois de recherche sur la nature et les technologies (FQRNT), the Natural Sciences and Engineering Research Council of Canada (NSERC), and the Fonds de recherche en santé du Québec (FRSQ). G.W. acknowledges the financial support from the National Natural Science Foundation of China (Grant No. 11074047). Calculations were done on the supercomputers of Calcul Québec. The authors thank Rozita Laghaei for helpful discussions.

REFERENCES

- (1) Selkoe, J. D. *Nature* **2003**, *426*, 900–904.
- (2) Soto, C. *Nat. Rev. Neurosci.* **2003**, *4*, 49–60.
- (3) Ross, C. A.; Poirier, M. A. *Nat. Rev. Mol. Cell Biol.* **2005**, *6*, 891–898.
- (4) Gatchel, J. R.; Zoghbi, H. Y. *Nat. Rev. Genet.* **2005**, *6*, 743–755.
- (5) Orr, H. T.; Zoghbi, H. Y. *Annu. Rev. Neurosci.* **2007**, *30*, 575–621.
- (6) Bates, G. P. *Nat. Rev. Genet.* **2005**, *6*, 768–773.
- (7) Hands, S. L.; Wyttenbach, A. *Acta Neuropathol.* **2010**, *120*, 419–437.
- (8) Mangiarini, L.; Sathasivam, K.; Seller, M.; Cozens, B.; Harper, A.; Hetherington, C.; Lawton, M.; Trotter, Y.; Lehrach, H.; Davies, S. W.; et al. *Cell* **1996**, *87*, 493–506.
- (9) Wetzel, R. J. *Mol. Biol.* **2012**, *421*, 466–490.
- (10) Ross, C. A.; Poirier, M. A.; Wanker, E. E.; Amzel, M. *Proc. Natl. Acad. Sci. U.S.A.* **2003**, *100*, 1–3.
- (11) Perutz, M. F. *Mol. Med.* **1995**, *1*, 718–721.
- (12) Perutz, M. F.; Finch, J. T.; Berriman, J.; Lesk, A. *Proc. Natl. Acad. Sci. U.S.A.* **2002**, *99*, 5591–5595.
- (13) Sikorski, P.; Atkins, E. *Biomacromolecules* **2005**, *6*, 425–432.
- (14) Thakur, A. K.; Wetzel, R. *Proc. Natl. Acad. Sci. U.S.A.* **2002**, *99*, 17014–17019.
- (15) Zhang, Q. C.; Yeh, T.-L.; Leyva, A.; Frank, L. G.; Miller, J.; Kim, Y. E.; Langen, R.; Finkbeiner, S.; Amzel, M. L.; Ross, C. A.; et al. *J. Biol. Chem.* **2011**, *286*, 8188–8196.
- (16) Sharma, D.; Shinchuk, L. M.; Inouye, H.; Wetzel, R.; Kirschner, D. A. *Proteins: Struct., Funct., Bioinf.* **2005**, *61*, 398–411.
- (17) Schneider, R.; Schumacher, M. C.; Mueller, H.; Nand, D.; Klaukien, V.; Heise, H.; Riedel, D.; Wolf, G.; Behrmann, E.; Raunser, S.; et al. *J. Mol. Biol.* **2011**, *412*, 121–136.
- (18) Jayaraman, M.; Kodali, R.; Sahoo, B.; Thakur, A. K.; Mayasundari, A.; Mishra, R.; Peterson, C. B.; Wetzel, R. *J. Mol. Biol.* **2012**, *415*, 881–899.
- (19) Chen, S.; Ferrone, F. A.; Wetzel, R. *Proc. Natl. Acad. Sci. U.S.A.* **2002**, *99*, 11884–11889.
- (20) Chen, S.; Berthelie, V.; Yang, W.; Wetzel, R. *J. Mol. Biol.* **2001**, *311*, 173–182.
- (21) Kar, K.; Jayaraman, M.; Sahoo, B.; Kodali, R.; Wetzel, R. *Nat. Struct. Mol. Biol.* **2011**, *18*, 328–337.
- (22) Stork, M.; Giese, A.; Kretschmar, H. A.; Tavan, P. *Biophys. J.* **2005**, *88*, 2442–2451.
- (23) Chopra, M.; Reddy, A. S.; Abbott, N. L.; de Pablo, J. J. *J. Chem. Phys.* **2008**, *129*, 135102.
- (24) Khare, S. D.; Ding, F.; Gwanmesia, K. N.; Dokholyan, N. V. *PLoS Comput. Biol.* **2005**, *1*, e30.
- (25) Marchut, A. J.; Hall, C. K. *Proteins: Struct., Funct., Bioinf.* **2007**, *66*, 96–109.
- (26) Zanuy, D.; Gunasekaran, K.; Lesk, A. M.; Nussinov, R. *J. Mol. Biol.* **2006**, *358*, 330–345.
- (27) Esposito, L.; Paladino, A.; Pedone, C.; Vitagliano, L. *Biophys. J.* **2008**, *94*, 4031–4040.
- (28) Vitalis, A.; Lyle, N.; Pappu, R. V. *Biophys. J.* **2009**, *97*, 303–311.
- (29) Vitalis, A.; Wang, X.; Pappu, R. V. *J. Mol. Biol.* **2008**, *384*, 279–297.
- (30) Klein, F. A. C.; Pastore, A.; Masino, L.; Zeder-Lutz, G.; Nierengarten, H.; Oulad-Abdelghani, M.; Altschuh, D.; Mandel, J.-L.; Trotter, Y. *J. Mol. Biol.* **2007**, *371*, 235–244.
- (31) Nozaki, K.; Osamu, O.; Hiroki, T.; Shoji, T. *Neuroreport* **2001**, *12*, 3357–3364.
- (32) Robertson, A. L.; Bate, M. A.; Buckle, A. M.; Bottomley, S. P. *J. Mol. Biol.* **2011**, *413*, 879–887.
- (33) Atwal, R. S.; Xia, J.; Pinchev, D.; Taylor, J.; Epan, R. M.; Truant, R. *Hum. Mol. Genet.* **2007**, *16*, 2600–2615.
- (34) Rockabrand, E.; Slepko, N.; Pantalone, A.; Nukala, V. N.; Kazantsev, A.; Marsh, J. L.; Sullivan, P. G.; Steffan, J. S.; Sensi, S. L.; Thompson, L. M. *Hum. Mol. Genet.* **2007**, *16*, 61–77.
- (35) Darnell, G.; Orgel, J. P. R. O.; Pahl, R.; Meredith, S. C. *J. Mol. Biol.* **2007**, *374*, 688–704.
- (36) Liebman, S. W.; Meredith, S. C. *Nat. Chem. Biol.* **2010**, *6*, 7–8.

- (37) Thakur, A. K.; Jayaraman, M.; Mishra, R.; Thakur, M.; Chellgren, V. M.; Byeon, I.-J. L.; Anjum, D. H.; Kodali, R.; Creamer, T. P.; Conway, J. F.; et al. *Nat. Struct. Mol. Biol.* **2009**, *16*, 380–389.
- (38) Tam, S.; Spiess, C.; Auyeung, W.; Joachimiak, L.; Chen, B.; Poirier, M. A.; Frydman, J. *Nat. Struct. Mol. Biol.* **2009**, *16*, 1279–1286.
- (39) Saunders, H. M.; Bottomley, S. P. *J. Mol. Biol.* **2009**, *22*, 447–451.
- (40) Fiumara, F.; Luana, F.; Kandel, E. R.; Hendrickson, W. A. *Cell* **2010**, *143*, 1121–1135.
- (41) Kelley, N. W.; Huang, X.; Tam, S.; Spiess, C.; Frydman, J.; Pande, V. S. *J. Mol. Biol.* **2009**, *388*, 919–927.
- (42) Rossetti, G.; Cossio, P.; Laio, A.; Carloni, P. *FEBS Lett.* **2011**, *585*, 3086–3089.
- (43) Kim, M. W.; Chelliah, Y.; Kim, S. W.; Otwinowski, Z.; Bezprozvanny, I. *Structure* **2009**, *17*, 1205–1212.
- (44) Dlugosz, M.; Trylska, J. *J. Phys. Chem. B* **2011**, *115*, 11597–11608.
- (45) Williamson, T. E.; Vitalis, A.; Crick, S. L.; Pappu, R. V. *J. Mol. Biol.* **2010**, *396*, 1295–1309.
- (46) Laghaei, R.; Mousseau, N. J. *J. Chem. Phys.* **2010**, *132*, 165102.
- (47) Krivov, G. G.; Shapovalov, M. V.; Dunbrack, R. L., Jr. *Proteins: Struct., Funct., Bioinf.* **2009**, *77*, 778–795.
- (48) Hess, B.; Kutzner, C.; van der Spoel, D.; Lindahl, E. *J. Chem. Theory Comput.* **2008**, *4*, 435–447.
- (49) van der Spoel, D.; Lindahl, E.; Hess, B.; Groenhof, G.; Mark, A. E.; Berendsen, H. J. C. *J. Comput. Chem.* **2005**, *26*, 1701–1719.
- (50) Lindahl, E.; Hess, B.; van der Spoel, D. *J. Mol. Model.* **2001**, *7*, 306–317.
- (51) Berendsen, H. J. C.; van der Spoel, D.; van Drunen, R. *Comput. Phys. Commun.* **1995**, *91*, 43–56.
- (52) Kaminski, G. A.; Friesner, R. A.; Tirado-Rives, J.; Jorgensen, W. L. *J. Phys. Chem. B* **2001**, *105*, 6474–6487.
- (53) Jorgensen, W. L.; Maxwell, D. S.; Tirado-Rives, J. *J. Am. Chem. Soc.* **1996**, *118*, 11225–11236.
- (54) Jorgensen, W. L.; Chandrasekhar, J.; Madura, J. D.; Impey, R. W.; Klein, M. L. *J. Chem. Phys.* **1983**, *79*, 926–935.
- (55) Hess, B.; Bekker, H.; Berendsen, H. J. C.; Fraaije, J. G. E. M. *J. Comput. Chem.* **1997**, *18*, 1463–1472.
- (56) Miyamoto, S.; Kollman, P. *J. Comput. Chem.* **1992**, *13*, 952–962.
- (57) Bussi, G.; Donadio, D.; Parrinello, M. *J. Chem. Phys.* **2007**, *126*, 014101.
- (58) Parrinello, M.; Rahman, A. *J. Appl. Phys.* **1981**, *52*, 7182.
- (59) Nose, S.; Klein, M. L. *Mol. Phys.* **1983**, *50*, 1055–1076.
- (60) Darden, T.; York, D.; Pedersen, L. *J. Chem. Phys.* **1993**, *98*, 10089–10092.
- (61) Essmann, U.; Perera, L.; Berkowitz, M. L.; Darden, T.; Lee, H.; Pedersen, L. *J. Chem. Phys.* **1995**, *103*, 8577–8592.
- (62) Oostenbrink, C.; Villa, A.; Mark, A. E.; Van Gunsteren, W. F. *J. Comput. Chem.* **2004**, *25*, 1656–1676.
- (63) MacKerell, J. A. D.; Feig, M.; Brooks, C. L., III. *J. Comput. Chem.* **2004**, *25*, 1400–1415.
- (64) MacKerell, A. D., Jr.; Bashford, D.; Bellott, M.; Dunbrack, R. L., Jr.; Evanseck, J. D.; Field, M. J.; Fischer, S.; Gao, J.; Guo, H.; Ha, S.; et al. *J. Phys. Chem. B* **1998**, *102*, 3586–3616.
- (65) Lindorff-Larsen, K.; Piana, S.; Palmo, K.; Maragakis, P.; Klepeis, J. L.; Dror, R. O.; Shaw, D. E. *Proteins: Struct., Funct., Bioinf.* **2010**, *78*, 1950–1958.
- (66) Eisenhaber, F.; Lijnzaad, P.; Argos, P.; Sander, C.; Scharf, M. *J. Comput. Chem.* **1995**, *16*, 273–284.
- (67) Frishman, D.; Argos, P. *Proteins: Struct., Funct., Genet.* **1995**, *23*, 566–579.
- (68) Huet, A.; Derreumaux, P. *Biophys. J.* **2006**, *91*, 3829.
- (69) Miettinen, M. S.; Knecht, V.; Monticelli, L.; Ignatova, Z. *J. Phys. Chem. B* **2012**, *116*, 10259–10265.
- (70) Ogawa, H.; Nakano, M.; Watanabe, H.; Starikov, E. B.; Rothstein, S. M.; Tanaka, S. *Comput. Biol. Chem.* **2008**, *32*, 102–110.
- (71) Nakano, M.; Watanabe, H.; Starikov, E. B.; Rothstein, S. M.; Tanaka, S. *Interdiscip. Sci.: Comput. Life Sci.* **2009**, *1*, 21–29.
- (72) Tycko, R. Q. *Rev. Biophys.* **2006**, *39*, 1–55.
- (73) Paravastu, A. K.; Petkova, A. T.; Tycko, R. *Biophys. J.* **2006**, *90*, 4618–4629.
- (74) Petkova, A. T.; Leapman, R. D.; Guo, Z.; Yau, W.-M.; Mattson, M. P.; Tycko, R. *Science* **2005**, *307*, 262–265.
- (75) Zhang, R.; Hu, X.; Khant, H.; Ludtke, S. J.; Chiu, W.; Schmid, M. F.; Frieden, C.; Lee, J.-M. *Proc. Natl. Acad. Sci. U.S.A.* **2009**, *106*, 4653–4658.
- (76) Miller, Y.; Ma, B.; Tsai, C.-J.; Nussinov, R. *Proc. Natl. Acad. Sci. U.S.A.* **2010**, *107*, 14128–14133.
- (77) Paravastu, A. K.; Leapman, R. D.; Yau, W.-M.; Tycko, R. *Proc. Natl. Acad. Sci. U.S.A.* **2008**, *105*, 18349–18354.
- (78) Lee, C. C.; Walters, R. H.; Murphy, R. M. *Biochemistry* **2007**, *46*, 12810–12820.
- (79) Vitalis, A.; Pappu, R. V. *Biophys. Chem.* **2011**, *159*, 14–23.
- (80) Barton, S.; Jacak, R.; Khare, S. D.; Ding, F.; Dokholyan, N. V. *J. Biol. Chem.* **2007**, *282*, 25487–25492.
- (81) Marchut, A. J.; Hall, C. K. *Biophys. J.* **2006**, *90*, 4574–4584.
- (82) Lakhani, V. V.; Ding, F.; Dokholyan, N. V. *PLoS Comput. Biol.* **2010**, *6*, e1000772.
- (83) Freddolino, P. L.; Liu, F.; Gruebele, M.; Schulten, K. *Biophys. Lett.* **2008**, L75–L77.
- (84) Freddolino, P. L.; Park, S.; Roux, B.; Schulten, K. *Biophys. J.* **2009**, *96*, 3772–3780.
- (85) Mittal, J.; Best, R. B. *Biophys. Lett.* **2010**, *99*, L26–L28.
- (86) Piana, S.; Lindorff-Larsen, K.; Shaw, D. E. *Biophys. J.* **2011**, *100*, L47–L49.
- (87) Best, R. B.; Hummer, G. *J. Phys. Chem. B* **2009**, *113*, 9004–9015.
- (88) Lindorff-Larsen, K.; Maragakis, P.; Piana, S.; Eastwood, M. P.; Dror, R. O.; Shaw, D. E. *PLoS One* **2012**, *7*, e32131.